RSC Advances

ROYAL SOCIETY OF CHEMISTRY

PAPER

View Article Online
View Journal | View Issue

Check for updates

Cite this: *RSC Adv.*, 2026, **16**, 261

# *In situ* synthesis of aluminum/copper-doped carbon dots from magnetite graphene oxide-carboxymethyl cellulose-2-acrylamido-2-methyl-1-propanesulfonic acid hydrogel and their electrical characterization

Hebat-Allah S. Tohamy, [a] Mohamed El-Sakhawy *[a] and Azhar M. Elwan[b]

Received 9th October 2025
Accepted 16th December 2025

DOI: 10.1039/d5ra07705b

rsc.li/rsc-advances

The recycling of agricultural residues into functional nanomaterials offers a sustainable pathway for next-generation electronics and energy devices. In this study, sugarcane bagasse was valorized to synthesize aluminum/copper-doped carbon dots (Al/Cu-CDs) embedded in a magnetite-graphene oxide ($Fe_3O_4$-GO) reinforced carboxymethyl cellulose–2-acrylamido-2-methyl-1-propanesulfonic acid (CMC-AMPS) hydrogel by a sustainable, *in situ* one-pot microwave-assisted approach. The sequential doping of Al and Cu ions in the carbon dots enables precise tuning of electronic structure, leading to significantly enhanced electrical conductivity, permittivity, and charge storage capacity compared to undoped analogs. Physicochemical characterizations, including FTIR, TEM, and UV-vis spectroscopy, confirm uniform nanoparticle distribution, and nanoscale features, with particle sizes in the range of 2.8–5.4 nm for Cu-CDs and 5.0–5.4 nm for Al/Cu-CDs. The resulting composite exhibits enhanced multifunctionality, combining magnetic, conductive, and biocompatible properties. Electrical measurements revealed a four-decade increase in conductivity and permittivity upon aluminum doping, alongside reduced impedance, indicating superior charge mobility. These findings demonstrate that the sustainable Al/Cu–$Fe_3O_4$/GO-CMC-AMPS nanocomposite is a promising candidate for applications in energy storage, supercapacitors, and biosensing applications.

## Introduction

Recent development in nanomaterials have enabled the design of multifunctional materials with tailored properties for applications in electronics, sensors, water treatment, and energy storage.[1–6] Among these materials, carbon dots (CDs) have gained considerable attention due to their unique optical and electrical properties, biodegradability, low toxicity, and facile preparation.[7–11] Typically, CDs are quasi-spherical particles with sizes between in the range of 1–10 nm, derived from diverse carbon-based precursors.[12,13] Their functionality can be further expanded their potential by combining them with other materials, such as metal oxides and hydrogels, leading to high-performance composites with enhanced performance.[14] Building on previous work where carboxymethyl cellulose/2-acrylamido-2-methyl-1-propane sulfonic acid (CMC/AMPS) hydrogel demonstrated strong adsorption and structural properties for water treatment,[15] this study employed this biopolymeric matrix as a sustainable platform for embedding multifunctional nanostructures. This article explores an innovative method to improve the functional properties of carbon dots through the *in situ* synthesis of aluminum/copper-doped carbon dots (Al/Cu-CDs) within a magnetite graphene oxide matrix ($Fe_3O_4$-GO) reinforced CMC-AMPS hydrogel. We highlight the methodology, properties, and potential applications of this novel composite material.

Each component of the hybrid system was deliberately chosen to address limitations of conventional doped CDs. The synthesis process begins with the extraction of carboxymethyl cellulose (CMC), a cellulose derivative widely used across industries due to its biocompatibility, biodegradability, and ability to form hydrogels.[16,17] The use of CMC as a polymer matrix in the synthesis nanomaterials offers several advantages as enhancing nanoparticle stability and dispersion, crucial for applications in drug delivery, sensors, and catalysis.[18] Notably, CMC is derived from sugarcane bagasse, a renewable agricultural waste rich in polysaccharides. The utilization of renewable feedstocks like sugarcane not only minimizes waste but also focuses on sustainable approaches in materials science. By treating bagasse with alkali and etherification, the hydroxyl groups are replaced with carboxymethyl groups, yielding

---

[a] *Cellulose and Paper Department, National Research Centre, Dokki, Giza, 12622, Egypt. E-mail: elsakhawy@yahoo.com*

[b] *Dept. of Biochemistry, National Research Centre, 33 El Bohouth st, Dokki, Giza, P.O. 12622, Egypt*

CMC.[19–23] The use of such biopolymer-derived precursors, such as chitosan-derived carbon dots, has been shown to influence the morphology, optical properties, and surface modulation of the resulting CDs, highlighting the importance of the precursor choice in determining final material characteristics.[24]

Graphene oxide (GO), provides a high surface area, mechanical strength, and functional groups (hydroxyl, epoxy, carboxyl), which enable surface modifications.[25] GO is commonly synthesized by oxidizing graphite, but in this study, we utilize sugarcane bagasse as the source material.[26] The approach is distinctive in simultaneously deriving both carbon sources (CMC and GO) and the hydrogel matrix from renewable sugarcane bagasse, thus coupling waste valorization with advanced materials synthesis. The oxidation reaction introduces oxygen-containing functional groups, making GO hydrophilic and easily dispersible in aqueous solutions.[27] Furthermore, controlled atmospheric conditions and the use of ferrocene refine its structure, optimizing its electronic and mechanical properties.[28] GO is frequently employed as a precursor for the synthesis of other nanomaterials, such as carbon dots, because it can undergo a number of various chemical reactions.[29] GO's excellent electrical and thermal conductivity, combined with its easy functionalization, makes it a prime candidate for advanced composites used in energy storage, sensors, and catalysis.[30,31]

Magnetite ($Fe_3O_4$) is a magnetic nanoparticle that has been extensively investigated for applications in drug delivery, environmental remediation, and magnetic resonance imaging.[32] By combining $Fe_3O_4$ with GO, magnetite-graphene oxide ($Fe_3O_4$-GO) composite was created, which exhibit strong magnetic responsiveness, high surface area, and robust interactions between $Fe_3O_4$ and GO components.[33] These properties make them particularly valuable for pollutant removal in environmental monitoring.[34,35] The *in situ* synthesis of $Fe_3O_4$-GO nanoparticles *via* chemical co-precipitation from $Fe^{3+}$ and $Fe^{2+}$ precursors with GO suspensions, forcing synergistic properties of both materials such as enhanced dispersibility and magnetic performance, which when embedded in the hydrogel matrix ($Fe_3O_4$-GO-CMC-AMPS), forms a robust multifunctional platform.[36]

Doping carbon dots with metal ions like copper (Cu) and aluminum (Al) can significantly alter their optical, electronic, and catalytic properties. Copper doping enhances fluorescence, charge transport, and catalytic activity, while aluminum doping improves stability, conductivity, and photoluminescence efficiency of the dots.[37] The doping process introduces new electronic states to the carbon dots, which can result in enhanced performance in a wide range of applications, such as sensing, energy storage, and catalysis.[38] The strategy of co-doping with multiple metal ions is a proven method to precisely tune the material's properties, as demonstrated in studies involving Al and Na co-doped thin films for various applications.[39] Furthermore, the use of metal-doped carbon dots, such as Cu, N-doped CDs, has been successfully explored for applications like corrosion inhibition, with detailed characterization using techniques like XPS and TEM being essential to understand the doping mechanism and resulting performance.[40]

Although metal-doped CDs and hydrogel composites have been previously reported, most studies focus on single-ion doping or require multi-step synthesis. Copper ions are introduced during this process to form Cu–$Fe_3O_4$, which further improves the electronic conductivity of the resultant Cu–$Fe_3O_4$/CDs.[41] This doping process is significant as it not only enhances the photoluminescence efficiency but also increases the charge transport, making it an attractive candidate for electronic applications.[42] The present work employs a sequential *in situ* doping strategy during a microwave-assisted one-pot synthesis, enabling uniform metal ion distribution and precise tuning of CD properties. This strategy differentiates our composite by reducing synthesis complexity, energy consumption, and waste generation, which aligns with sustainable material development goals. The final step involves aluminum doping, where Al ions are incorporated carefully into Cu–$Fe_3O_4$/CDs to ensure uniform distribution within the carbon dot structure. Aluminum doping is expected to modulate the electronic structure of the carbon dots to enhance their stability, conductivity and performance in electronic devices.[38] The resulting Al/Cu–$Fe_3O_4$/CDs benefit from the synergistic effects of aluminum and copper doping, combined with the magnetic, graphitic structure from $Fe_3O_4$-GO.

Regarding application motivation, the dual Al/Cu doping and hydrogel embedding are specifically engineered to improve electrical conductivity and charge storage capacity, targeting energy storage devices and sensors that require materials combining electronic performance with robust, biocompatible supports. The conductivity of the synthesized carbon dots is of particular interest, as it directly relates to their use in conducting films, flexible electronic devices, sensors, and as electron transport layers in solar cells and light-emitting diodes (LEDs).[43] In environmental science, the composite may find application in water treatment and pollution monitoring, where magnetite enhances the easy pollutant removal while carbon dots function as heavy metal sensors.

In previous work, the synthesis and characterization of $FeAl_xFe_2\text{-}xO_4$ ($x$ = 0.2, 0.4, 0.6) have been investigated. In dielectric properties, AC conductivity decreased with the increase of $Al^{3+}$ doping at 473 K, which has been clarified as a hopping mechanism. Also, variation of dielectric loss, tan $\delta$, dielectric permittivity ($\varepsilon'$), and ac conductivity ($\sigma_{ac}$) with temperature and frequency can be elucidated on the basis of Maxwell–Wagner type of hopping mechanism and interfacial polarization. DC resistivity decreased with increasing temperature, signifying that the substituted ferrites have a semiconductor behavior.[44]

The electrical properties of DEG-stabilized $CuxFe_1\text{–}xFe_2\text{–}xO_4$ NPs at a temperature of 180 °C have been investigated by Amir *et al.* They found that the $\sigma_{dc}$ relies on the concentration of $Cu^{2+}$ ions and temperature. The maximum $\sigma_{dc}$ value was $1.85 \times 10^{-7}$ S cm$^{-1}$ for $x = 0.0$ at 120 °C. The DEG-stabilized $CuxFe_1\text{–}xFe_2O_4$ NPs displayed relatively high dielectric permittivity (between $10^2$ and $10^5$). The detected properties of this composite showed varied biomedical applications, and a metal ion separator from wastewater.[45]

The novelty of this work lies in the synergistic *in situ* synthesis of Al/Cu-doped CDs within the $Fe_3O_4$-GO-CMC-AMPS hydrogel using a one-pot, microwave-assisted method from a single renewable precursor (sugarcane bagasse). This eco-friendly approach reduces complexity, energy use, and waste compared to traditional separate syntheses. The final composite integrates magnetic, electrical, adsorption, and biocompatible properties, enabling high-performance multifunctional composite. Further research and development in this area will likely lead to the creation of new and innovative devices and technologies that address pressing societal challenges.

## Material and methods

### Materials

The sugarcane bagasse (SCB) was obtained from the Paper Industry Quena Company, Egypt. 2-Acrylamido-2-methyl-1-propane-sulfonic acid (AMPS) was purchased from Alfa Aesar. Ferrocene (F) was obtained from Sisco Research Lab Ltd (SRL), India. Both *N*, *N*′-methylenebisacrylamide (MBA), and potassium persulfate (KPS) were obtained from Sigma-Aldrich. Chemicals, reagents, and substrates employed in this study were of analytical grade and were used as received without any additional purification.

### Preparation of magnetite graphene oxide ($Fe_3O_4$-GO) from SCB

Graphene oxide was produced through the oxidation of sugarcane bagasse (SCB) using a specific reagent (F) at 300 °C in a controlled atmosphere. This method involved heating a combination of SCB (0.5 g) and F (0.1 g) at 300 °C for 10 minutes within a furnace. The resulting material, denoted as GO, constituted the graphene oxide, which was recovered as a black powder under standard laboratory conditions.[24,25] An aqueous dispersion of graphene oxide (GO, 25 mg in 50 mL of deionized water) was subjected to 30 minutes of ultrasonication. Concurrently, a precursor solution (100 mL) containing $Fe^{3+}$ and $Fe^{2+}$ ions in a 2 : 1 molar ratio was pre-hydrolyzed by slowly adding a 1 M NaOH aqueous solution under continuous agitation. Upon reaching a pH of 4, the GO dispersion was slowly introduced into the iron solution and stirred for another 30 minutes to ensure homogeneity. The pH of the resulting mixture was then raised to 11–12 by continued NaOH addition, followed by 30 minutes of stirring. The resulting magnetic graphene oxide (MGO) precipitate was isolated using magnetic separation, washed with deionized water and absolute ethanol, and subsequently dried at 60 °C in an oven. For comparative purposes, $Fe_3O_4$ nanoparticles were also synthesized using the same procedure but without the addition of GO.[15]

### Preparation of carboxymethyl cellulose (CMC)

SCB underwent hydrolysis with a dilute hydrochloric acid solution (1.5% based on SCB weight) at a liquid-to-solid ratio of 10 : 1 at 120 °C for 2 hours. The resulting pre-hydrolyzed SCB was then subjected to alkaline treatment using sodium hydroxide (20% of SCB weight) at 170 °C for 2 hours with a liquor ratio of 7 : 1. To remove the remaining lignin, the pre-treated bagasse was bleached with chlorous acid ($HClO_2$). Subsequently, mercerization of the cellulose was carried out using a 17.5% sodium hydroxide solution to eliminate any residual lignin and obtain pure α-cellulose. The α-cellulose was then reacted with monochloroacetic acid at 60 °C for 2 hours under agitation to produce carboxymethyl cellulose (CMC).[46]

### Preparation of the CMC-AMPS-$Fe_3O_4$-GO hydrogel

Following the formation of a uniform mixture, the temperature was raised to 60 °C, and a solution of potassium persulfate (0.24 g) in 5 mL of distilled water was introduced. Subsequently, the temperature was held at 65 °C for 10 minutes to initiate the formation of free radicals on the carboxymethyl cellulose (CMC) polymer backbones. An aqueous dispersion containing 2 g of $Fe_3O_4$-GO, 4 g of AMPS neutralized to pH 5.5 with aqueous NaOH, and 0.48 g of *N*, *N*′-methylenebisacrylamide was then added to the reaction mixture. The temperature was then maintained at 70 °C and pH 5.5 for a duration of 3 hours. The resulting hydrogel underwent rinsing with distilled water to remove unreacted water-soluble monomers, homopolymers, and the crosslinking agent. Subsequently, the hydrogel was frozen at −80 °C for 3 hours and then subjected to freeze-drying using a Christ-Alpha 1–2 LD Plus apparatus. The grafting of AMPS onto CMC, CMC with, and CMC with $Fe_3O_4$-GO were designated as $Fe_3O_4$-GO-CMC-AMPS.[15]

### Preparation of copper doped magnetite-CDs (Cu–$Fe_3O_4$/CDs) from CMC-AMPS- $Fe_3O_4$-GO

Copper-doped carbon dots (Cu-CDs) were prepared by adding 1.125 g of $CuNO_3$ to 0.52 g of the previously synthesized $Fe_3O_4$-GO-CMC-AMPS material in the presence of urea and sodium hydroxide. This mixture was then refrigerated for 1 day then treated with microwave irradiation at 700 W for 10 min. until the formation of Cu–$Fe_3O_4$/CDs.

### Preparation of aluminium/copper doped-CDs (Al/Cu–$Fe_3O_4$/CDs) from Cu–$Fe_3O_4$/CDs

The prepared Cu-CDs was treated with 1000 ppm $Al(NO_3)_3$ and treated with microwave irradiation at 700 W for 10 min. until the formation of Al/Cu–$Fe_3O_4$/CDs.

## Characterization

### Raman analysis

Raman spectra were recorded at an excitation laser wavelength of 532 nm using Raman confocal WITEC Focus Innovations Alpha-300 microscope.

### XRD analysis

The crystallinity was determined by Bruker D8 Advance X-ray diffractometer (Germany) using copper (Kα) radiation (1.5406 Å) at a 40 kV voltage and a 40 mA current. Crystallinity index (Cr.I. %) was calculated by the following equation:

$$\mathrm{Cr.I}(\%) = \frac{S_c}{S_t} \times 100 \quad (1)$$

where $S_t$ is the entire domain region and $S_c$ is the crystalline domain region. $\lambda$ is the wavelength of X-rays.[47,48]

The UV-vis absorption spectrum was recorded by a UV-vis spectrophotometer (JASCO V-630, Tokyo, Japan) using a 1 cm path length quartz cell.

FTIR spectra were recorded using a Mattson 5000 spectrometer (Unicam, United Kingdom) with KBr pellets. The crystallinity index (LOI) was calculated using eqn (2).

$$\mathrm{LOI} = \frac{A_{1425}}{A_{900}} \quad (2)$$

where $A_{1425}$ and $A_{900}$ refer to the FTIR absorbance at 1425 and 900 cm$^{-1}$, respectively. In addition, $A_{\mathrm{OH}}$ and $A_{\mathrm{CH}}$ refer to the FTIR absorbance of the OH and CH peaks, respectively.[49,50]

### Dielectric measurements

The samples' dielectric properties were performed using an alpha impedance analyser, which is part of the broadband dielectric spectrometer, BDS, from NovoControl Co., Germany. BDS also contains a quatro-system for temperature control using $N_2$ gas from a liquid $N_2$ dewar. NovoControl provides the software Win Deta, which completely controls the measurement process. The Authors used a frequency range from 0.1 Hz to 20 MHz and a temperature range from 30 °C to 90 °C. A ZGS active sample cell test interface for the Alpha-A analyzer series is a special version of the BDS1200 standard sample cell with optimized frequency performance. In addition, a two-electrode capacitor of gold-plated disks is used for sandwiching the sample. Samples were compressed into disk form with thickness of 1–2 mm and 1.2 cm diameter. ZGS system has its own performance-enhancing system and signal protection at the high and low frequency ranges. Data obtained were the average of three samples.

## Results and discussion

### Chemical characterization of GO

FTIR of GO has peaks between 3377 (O–H), 1654 (C=O), 1591 (C=C), 1456 (O–C=O), 1247 (C–O), and 1062 cm$^{-1}$ (C–O–C) (Fig. 1a). The XRD shows peaks at 2 = 9° (001) and 2 = 21° (002) which are typical signals for GO (Fig. 1b). The Raman spectroscopy showed G-band at 1582 cm$^{-1}$ and D-band at 1378 cm$^{-1}$.[24,51] The D-band appeared due to disorders.[24]

### Chemical characterization of the starting $Fe_3O_4$-GO-CMC-AMPS hydrogel

The FT-IR spectrum, Fig. 2a, of $Fe_3O_4$-GO showed peaks at 3330 cm$^{-1}$ (O–H), 1882 cm$^{-1}$ (C=O), 1583 cm$^{-1}$ (O=C–O), 1357 cm$^{-1}$ (C–O–C), and 599 cm$^{-1}$ (Fe–O). The CMC-AMPS hydrogel without $Fe_3O_4$-GO showed peaks at 3386 cm$^{-1}$ (N–H), 3321 cm$^{-1}$ (OH), 1635 cm$^{-1}$ (C=O), 1546 cm$^{-1}$ (C=C), 1411 cm$^{-1}$ (O=C–O), 1189 cm$^{-1}$ (C–O–C), and 1039 cm$^{-1}$ (S=O). The $Fe_3O_4$-GO-CMC-AMPS hydrogel with $Fe_3O_4$-GO showed the same peaks with additional peak at 555 cm$^{-1}$ (Fe–O) which prove the incorporation of $Fe_3O_4$-GO. TEM analysis for $Fe_3O_4$-GO exhibited a random distribution of platelets with width range between 7–7.07 nm and length range between 153–251 nm (Fig. 2b). The magnetization of the $Fe_3O_4$-GO was showed at Fig. 2c. The saturated magnetization (Ms, the maximum possible magnetization) was 26 emu g$^{-1}$ and remnant magnetization (Mr, the left in $Fe_3O_4$-GO when the external field is taken away) was 1 emu g$^{-1}$ of $Fe_3O_4$/N-CQDs. The XRD of $Fe_3O_4$-GO, Fig. 2d, showed peaks at $2\theta = 30.5°$, 34.3°, 43°, 47°, 53.1°, and 61.6°, which assign to their reflections including (220), (311), (400), (442), (511), and (440), respectively.[15]

The SEM surface morphology of CMC-AMPS hydrogel (Fig. 3a) showed a porous network structure with pore size range between 1.81–5.08 μm. This open morphology is indicative of efficient solvent exchange and potential for high adsorptive performance, as the interconnected pores facilitate mass transfer and accessibility to internal hydrogel domains.

Upon incorporation of $Fe_3O_4$-GO, the surface exhibits a noticeably denser, granular texture with reduced pore sizes, measured in the range of 1.61–2.38 μm, which prove $Fe_3O_4$-GO nanoparticles incorporation that block the pores, leading to reduced average pore diameter and diminished interconnectivity. Reduced pore volume may improve selectivity or retention during adsorption and can enhance structural stability, while still maintaining adequate micro-porosity for target applications.

EDX analysis confirms the elemental composition of the CMC-AMPS hydrogel and its $Fe_3O_4$-GO composite, highlighting successful incorporation of iron-based nanoparticles. For the pure CMC-AMPS hydrogel (Fig. 3b), the spectrum shows dominant peaks for carbon (C), oxygen (O), sodium (Na) from carboxymethyl groups, and sulfur (S) from AMPS sulfonate moieties, indicating the expected polymeric backbone without metallic contaminants.

In the $Fe_3O_4$-GO-CMC-AMPS composite (Fig. 3c), additional strong peaks for iron (Fe) emerge at approximately 3.3% atomic percentage, alongside minor signals from graphene oxide (GO) components, verifying uniform nanoparticle dispersion within the hydrogel matrix. This Fe content aligns with typical loadings for magnetic nanocomposites, enabling properties like magnetic separability and enhanced catalytic activity.

### TEM analysis for Cu–$Fe_3O_4$/CDs and Al/Cu–$Fe_3O_4$/CDs

The Cu–$Fe_3O_4$/CDs, TEM micrographs, Fig. 4a, revealed a nearly spherical particle with sizes ranging from 2.84–5.43 nm. The homogeneous nature and narrow size distribution provide compelling evidence that the copper ions actively participated in the nucleation and growth of the CDs rather than simply adsorbing to their surface. If the copper ions were merely adsorbed, heterogeneous aggregation and larger irregular structures would be expected. The presence of such small nanoparticles is highly advantageous, as quantum confinement effects become more pronounced in this size regime, potentially leading to enhanced optical and electronic properties. The selected area electron diffraction (SAED) pattern for the Cu–$Fe_3O_4$/CDs displays concentric diffuse rings rather than sharp

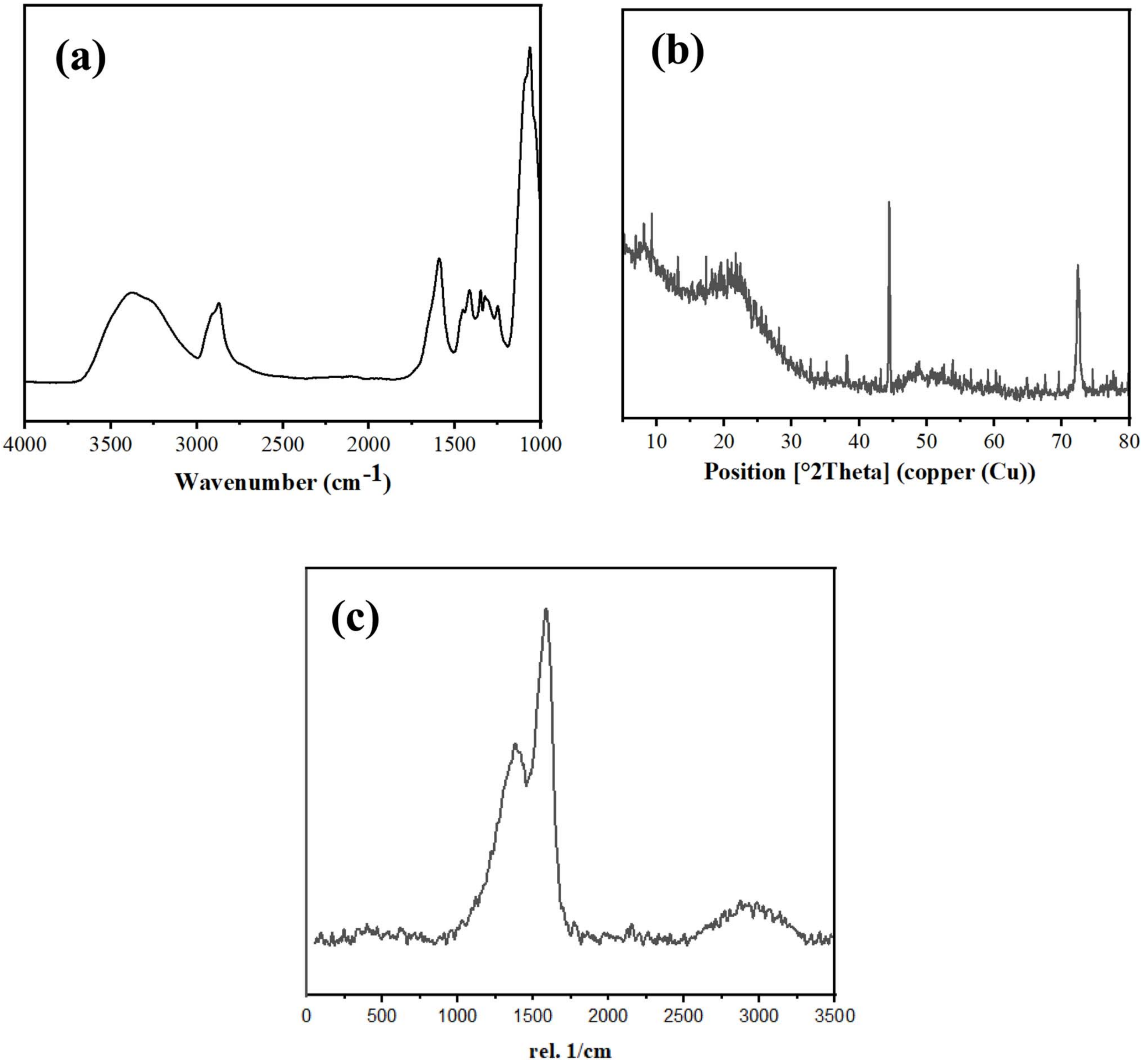

Fig. 1 (a) FTIR, (b) XRD, and (c) Raman spectroscopy of GO.

diffraction spots, characteristic of polycrystalline or partially amorphous nanostructures. The presence of multiple rings confirms that the Cu–$Fe_3O_4$/CDs possess crystalline domains embedded within an amorphous carbon matrix, confirming the successful integration of Cu and $Fe_3O_4$ components into a composite structure with carbon dots. The innermost bright ring can be attributed to the (111) plane of spinel $Fe_3O_4$, while subsequent rings may correspond to higher-order reflections. This hybrid structural configuration provides both crystallinity (beneficial for magnetic and catalytic performance) and amorphous carbon phases (supporting electronic/optical tunability), making the Cu–$Fe_3O_4$/CDs a promising multifunctional nanocomposite.

Upon further doping with aluminum to form Al/Cu–$Fe_3O_4$/CDs, Fig. 4b, a slight shift in the particle size distribution was observed, with particles ranging from 4.95–5.37 nm. This indicates a minor increase in the average particle size compared to Cu–$Fe_3O_4$/CDs, and notably, a further narrowing of the size distribution. The very tight range (0.42 nm difference between minimum and maximum) for Al/Cu–$Fe_3O_4$/CDs suggests that the incorporation of aluminum likely influences the growth kinetics and nucleation processes during the second microwave irradiation step, rather than mere surface adsorption, which typically leads to agglomeration. This observation strongly suggests that the $Al^{3+}$ ions integrated into the lattice, possibly acting as nucleation sites or as a stabilizing force that restricts the uncontrolled growth.

The SAED pattern for Al/Cu–$Fe_3O_4$/CDs exhibits well-defined concentric diffraction rings with uniform intensity, characteristic of polycrystalline materials and homogeneous particle

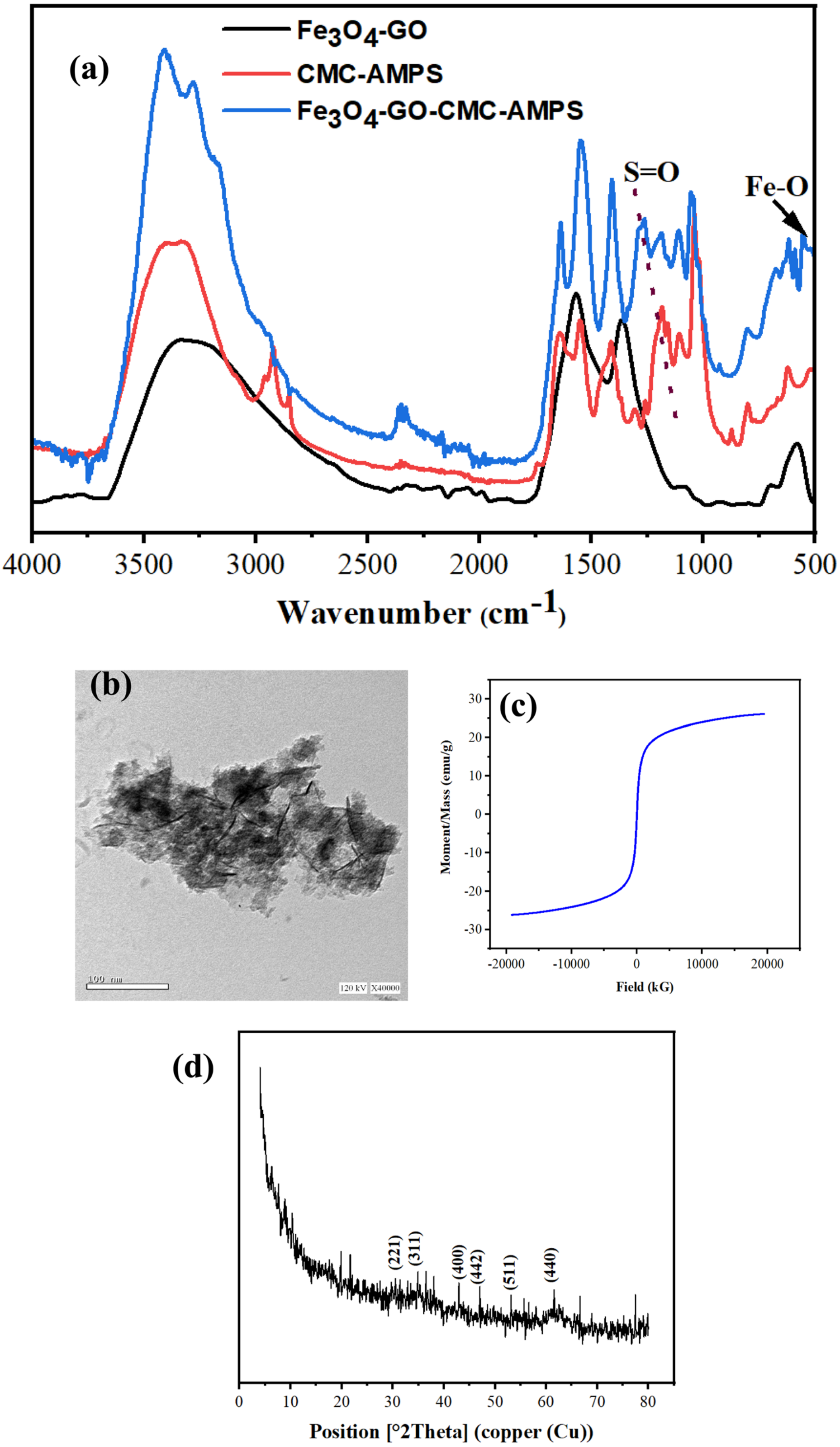

Fig. 2 (a) FTIR of $Fe_3O_4$-GO, CMC-AMPS hydrogel, and $Fe_3O_4$-GO-CMC-AMPS hydrogel; (b) TEM analysis of $Fe_3O_4$-GO (c) magnetisation of $Fe_3O_4$-GO; and (d) XRD of $Fe_3O_4$-GO.

dispersion. The absence of diffuse halos or spots further supports the presence of uniform, well-ordered nanoparticles, in agreement with the results of the size distribution observed in TEM. This validates that Al incorporation not only tunes the particle size but also maintains the crystalline integrity of the $Fe_3O_4$ lattice within the hybrid carbon dot framework.

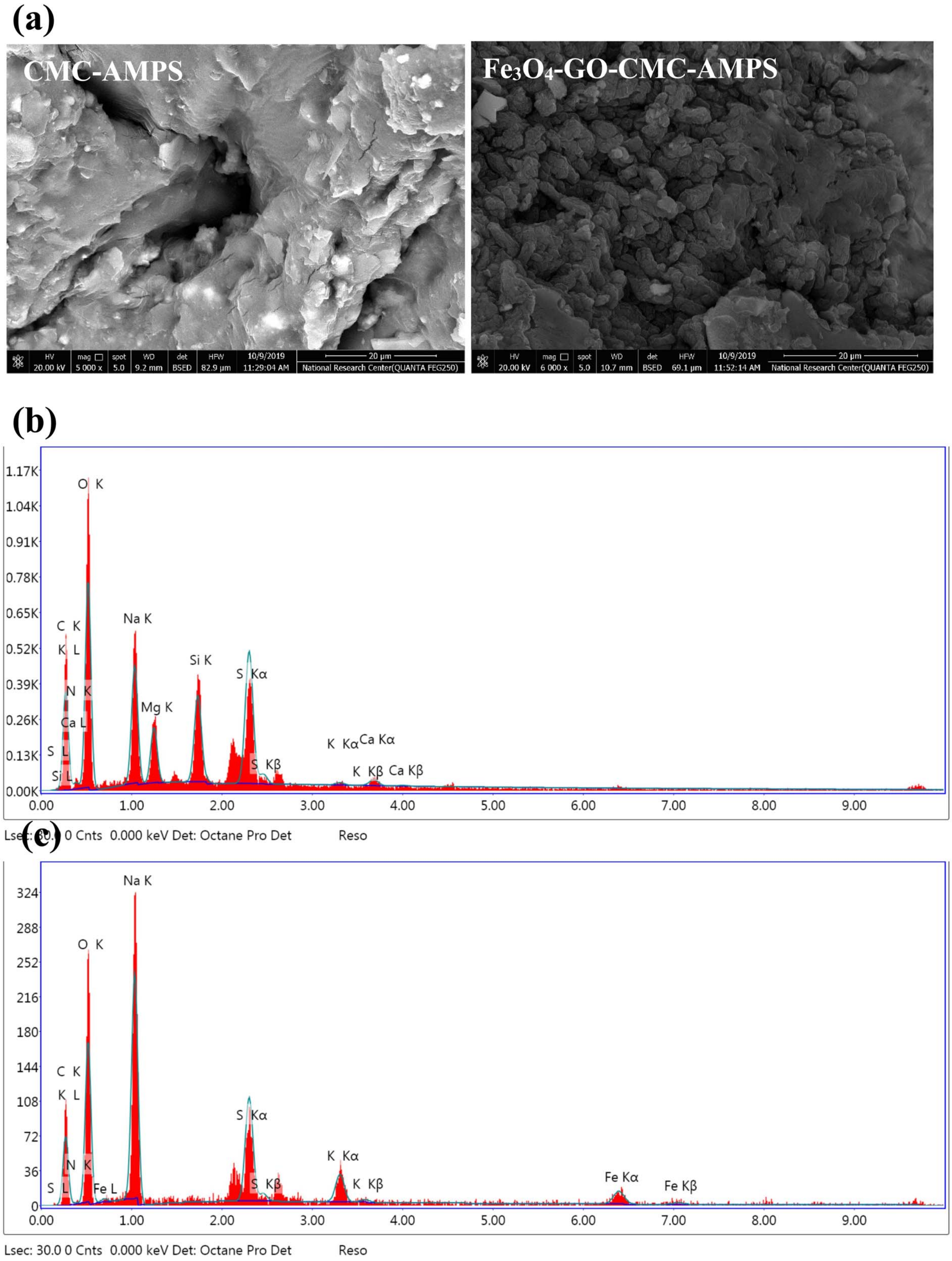

Fig. 3 (a) SEM analysis of CMC-AMPS hydrogel, and $Fe_3O_4$-GO-CMC-AMPS EDX for (b) CMC-AMPS hydrogel, and (c) $Fe_3O_4$-GO-CMC-AMPS.

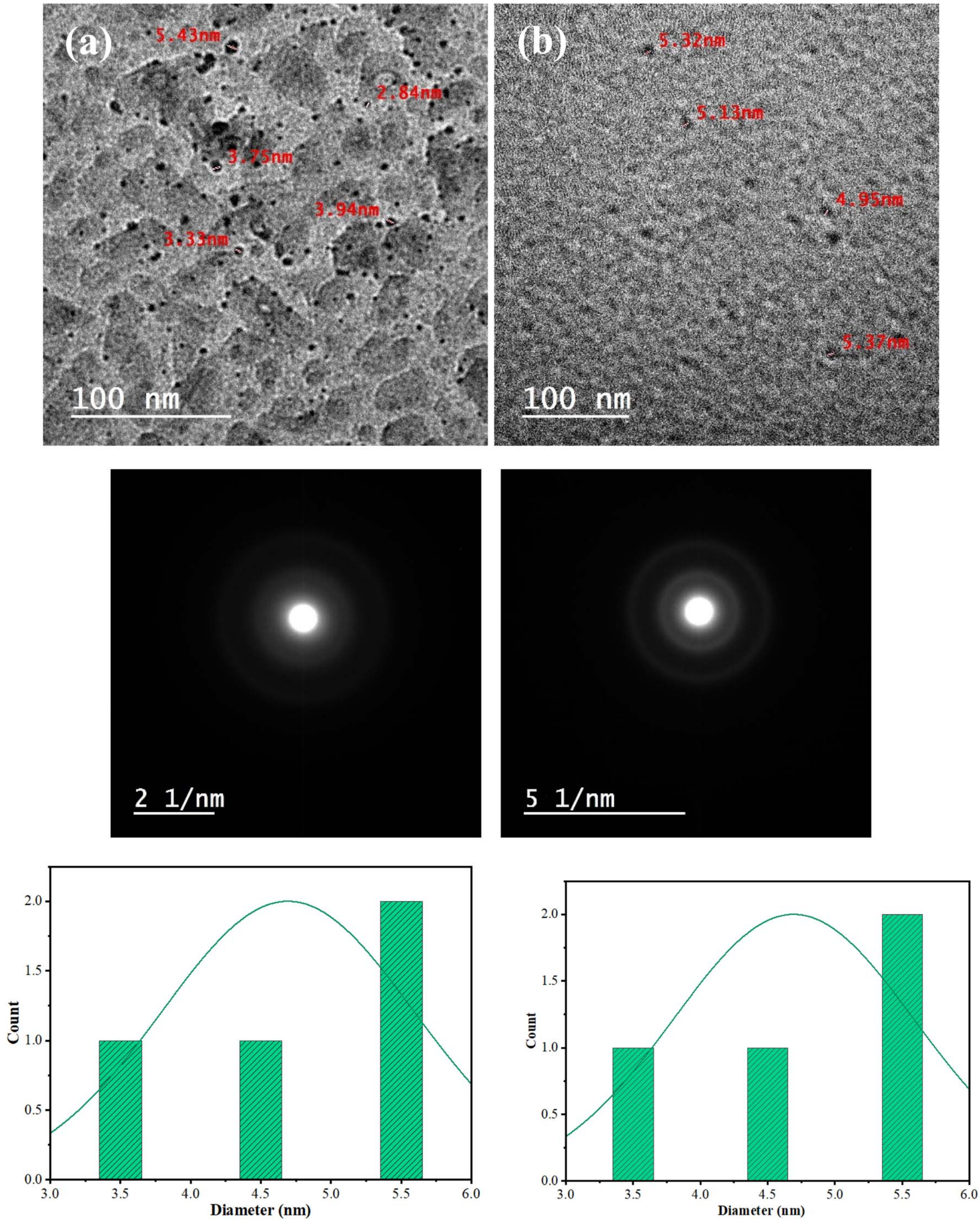

Fig. 4 TEM analysis and particle size histogram with SAED for (a) Cu–$Fe_3O_4$/CDs and (b) Al/Cu–$Fe_3O_4$/CDs.

## FTIR spectra and XRD analysis of Cu–$Fe_3O_4$/CDs and Al/Cu–$Fe_3O_4$/CDs

The FTIR spectra of the prepared Cu–$Fe_3O_4$/CDs and Al/Cu–$Fe_3O_4$/CDs showed peaks between 3319–3733 $cm^{-1}$ (O–H), 1585–1789 $cm^{-1}$ (C═O), 1417–1683 $cm^{-1}$ (C═C), 1332–1542 $cm^{-1}$ (O–C═O), and 1051–1110 $cm^{-1}$ (O–C–O). The peaks between 896–1047, 734–979, and 572–835 $cm^{-1}$ are related to Cu–O in Cu–$Fe_3O_4$/CDs and Al/Cu–$Fe_3O_4$/CDs.[52] A new peak appeared between 679 $cm^{-1}$ is related to the Al–O in Al/Cu–$Fe_3O_4$/CDs.[39] These peaks indicating chemical bonding beyond surface adsorption. The calculated LOI was 1.02 and 1.04 for Cu–$Fe_3O_4$/CDs and Al/Cu–$Fe_3O_4$/CDs which means the strong H-bonding (Fig. 5a).

The XRD spectroscopy for Cu–$Fe_3O_4$/CDs and Al/Cu–$Fe_3O_4$/CDs showed peaks at 2$\theta$ of 19.78° and 19.38°, respectively as shown in Fig. 5b due to the existence of graphitic carbon peaks

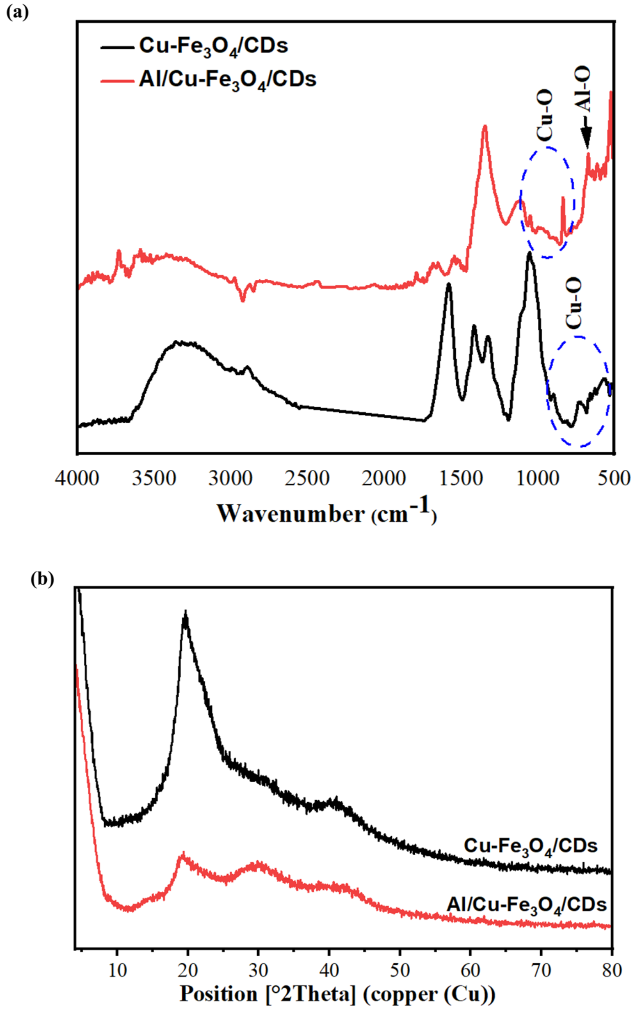

Fig. 5 FTIR spectra (a) and XRD (b) of Cu–Fe$_3$O$_4$/CDs and Al/Cu–Fe$_3$O$_4$/CDs.

of CDs. The diffraction peaks centered at around $2\theta = 20°$ is attributed to the turbostratic carbon phase and the broadness of the peaks due to amorphous nature of carbon in carbon dots.[53] The peak at 40.90° for Cu–Fe$_3$O$_4$/CDs and at 42.00° for Al/Cu–Fe$_3$O$_4$/CDs is associated with Cu (Ref. code 96-210-2368).[54] The XRD of Al/Cu–Fe$_3$O$_4$/CDs showed a more amorphous structure due to the disruption of the CDs lattice by the introduction of Al$^{3+}$ ions.[39] The calculated Cr.I was 43.70 and 39.27% for Cu–Fe$_3$O$_4$/CDs and Al/Cu–Fe$_3$O$_4$/CDs, respectively. The reduced crystallinity was referred to lattice disruption by Al ions, supporting lattice incorporation. The Cr.I decrease for Al/Cu–Fe$_3$O$_4$/CDs is also approved by TEM which show the low particle size.

## Bandgap determination

The UV-vis absorption of both samples, S1, Cu–Fe$_3$O$_4$/CDs, and S2, Al/Cu–Fe$_3$O$_4$/CDs, in Fig. 6 indicates no significant differences; they almost have the same spectrum. The wavelength in nm is converted into eV units of energy to obtain the band gap:

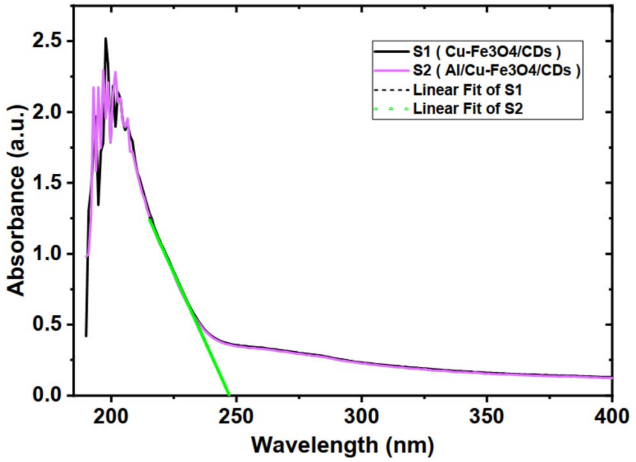

Fig. 6 UV-vis spectra of Cu–Fe$_3$O$_4$/CDs and Al/Cu–Fe$_3$O$_4$/CDs.

$$\text{Band gap energy(eV)} = h\nu(\text{eV}) = \frac{hC}{\lambda} = \frac{1239.8(\text{eV}x\text{nm})}{\lambda(\text{nm})}$$

Where, $h$: Plank's constant ($6.6261 \times 10^{-34}$ J × s), eV: $1.60218 \times 10^{-19}$ J, $C$ is the speed of light ($2.9979 \times 10^{8}$ m s$^{-1}$), and $\lambda$ (nm): wavelength in nanometers.[39,55]

By performing a tangent at the escalating absorption point, and extending the tangent line to intersect the $X$-axis, the wavelength and the band gap can be determined by applying the former energy equation. From the graph in Fig. 6, the fitting lines intersect the $X$-axis at 247.2 nm. This means the band gap energy for both samples is about 5.02 eV, which means the minimum energy required for an electron to jump from the valence band to the conduction band is 5.02 eV. This result places the composites into the insulators category. Despite both fitting lines for both composites almost coincide, intersecting the $X$-axis at the same point, which, alone, would falsely lead us to think that Al did not chemically alter the composition of the Cu–Fe$_3$O$_4$/CDs. However, Al atoms were both physically distributed homogeneously throughout the structure matrix, as indicated by the dielectric part, and chemically interacted with the composite, as pointed out by both FTIR and XRD investigations. This allowed the bypass of the band gap of the composite.

## Dielectric properties of the samples

As can be seen in Fig. 7, adding Al nitrates caused an elevation of permittivity, $\varepsilon'$, and loss, $\varepsilon''$, by about four decades for about five frequency decades. These data refer to the increment of charge storage, higher permittivity, and ability to fast release the stored charges as indicated by the high loss gain in $\varepsilon''$. The increase in permittivity is attributable to the vacancies left behind upon the evaporation of nitrates from the composite, which enabled the storage of more charges. While the increment in loss is due to the activity of the Al atoms left after the evaporation of nitrates, as each atom has one to three electrons, which are loosely bound.

In Fig. 8, data show the escalation of conductivity by four decades as a result of Al inclusion within the composite matrix.

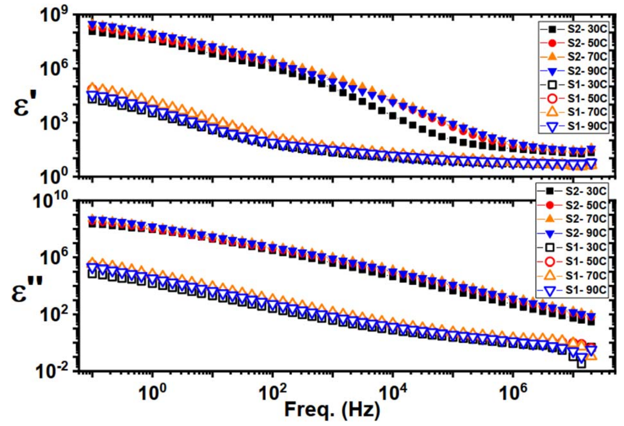

Fig. 7 Permittivity, $\varepsilon'$, and Loss, $\varepsilon''$, as frequency functions of S1: Cu–$Fe_3O_4$/CDs and S2: Al/Cu–$Fe_3O_4$/CDs at different temperatures.

The homogeneity of Al distribution within the sample ensured excess electrons and created an electron path through the composite. Consequently, causing an impedance reduction in the lower part of Fig. 8. Stability of real conductivity, $\sigma'$, and real impedance, $Z'$, values for S2, Al/Cu–$Fe_3O_4$/CDs, indicates the homogeneity of the Al distribution within the sample. It is worth to mention that the isolated undoped CDs has insulating ($\sigma < 10^{-6}$ S cm$^{-1}$, $\varepsilon' \sim 10^2$) which moderately enhanced for Cu-CDs: ($\sigma \sim 10^{-5}$ S cm$^{-1}$); while, full Al/Cu synergy shows four-decade enhancement ($\sigma$ up to $10^{-3}$ S cm$^{-1}$), isolating doping contributions.

Fig. 9 (upper part), the Cole–Cole plot for S1, Cu–$Fe_3O_4$/CDs, reveals two distinct relaxations manifested as two arcs with high real-impedance values (in MΩ), reflecting significant resistance and limited charge mobility indicative of semiconductor behaviour up to 70 °C. At 90 °C, the real impedance increases again, which may be due to temperature-induced reactions of Cu, Fe, and Al atoms with their surrounding environment, that disrupt charge transport pathways. This leads to a decrease in long-range charge mobility and charge carrier density, effectively switching the material's behavior from semiconductor to metallic-like at elevated temperature.

For S2, Al/Cu–$Fe_3O_4$/CDs (Fig. 9, lower part), the incorporation of Al markedly decreases the impedance values from the MΩ range to the hundreds of Ohm range, reflecting enhanced electrical conduction due to improved charge carrier concentration or mobility.

The impedance Cole–Cole plot indicates non-Debye relaxations, showing mixed behaviour of resistive and capacitive components. The presence of two relaxations reveals a low-frequency electrode and/or interfacial polarization, and the high-frequency relaxation indicates the grain relaxation. Significant impedance reduction is shown in S2 as well as a decrease in impedance with temperature, signifying semiconductor behaviour for the composite. Non-Debye relaxations centre is depressed below the *X*-axis, pointing out the existence of relaxation times' distribution, the complexity of the microstructure, and/or the multiple conduction processes occurring within the composite. The decrement of impedance in S2 indicated better conductivity based on structural differences between the two samples.

In Fig. 10, the corresponding conductivity plot shows very low conductivity (μS cm$^{-1}$ range) for S1, without a well-defined conduction mechanism, indicating that Cu atoms may be present in low amounts or they are chemically bound within the matrix, limiting free charge carriers.

On the other hand, the inclusion of Al in the composite matrix in S2, Al/Cu–$Fe_3O_4$/CDs, resulted in an enormous increase in conductivity (from μS cm$^{-1}$ for S1 to mS cm$^{-1}$ for S2), indicative of aluminum doping's critical role in facilitating electron transport by modifying the electronic structure and charge carrier pathways in the composite. Also led to clarification of two conduction mechanisms as shown in the lower part of Fig. 9 and the sub-fig within at 30 C. The smaller one appearing as a shoulder represents the electrode polarization at the electrode-sample interface, and the larger one represents the barrier hopping, as will be shown by the Jonscher conductivity fitting, Fig. 11 and 12. Increasing the temperature

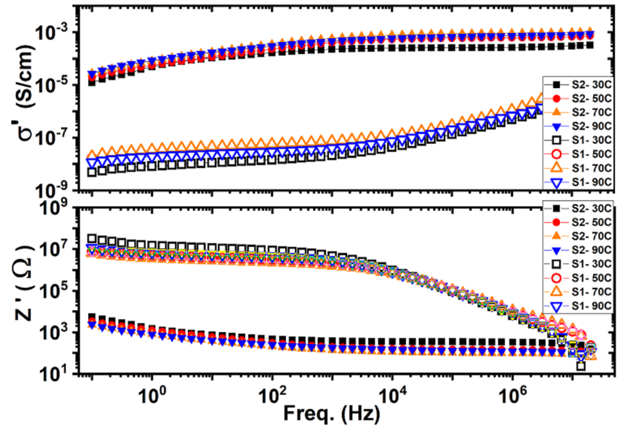

Fig. 8 Conductivity, $\sigma'$, and Impedance, $Z'$, as frequency functions of S1: Cu–$Fe_3O_4$/CDs and S2: Al/Cu–$Fe_3O_4$/CDs at different temperatures.

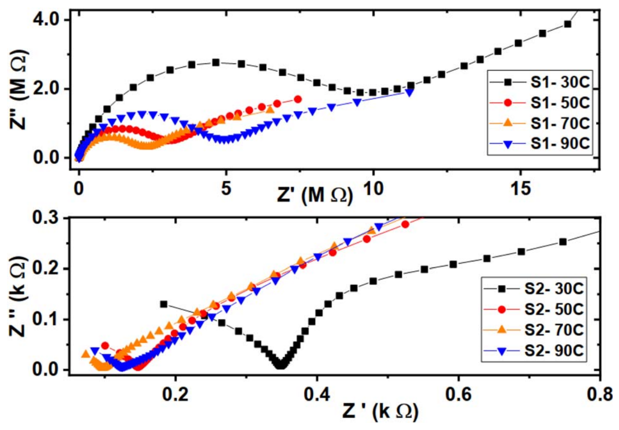

Fig. 9 Cole–Cole plot of impedance for S1: Cu–$Fe_3O_4$/CDs and S2: Al/Cu–$Fe_3O_4$/CDs at different temperatures.

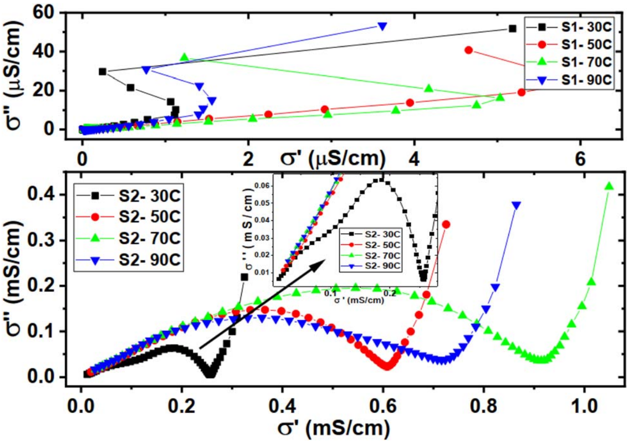

Fig. 10 Cole–Cole plot of conductivity for S1: Cu–$Fe_3O_4$/CDs and S2: Al/Cu–$Fe_3O_4$/CDs at different temperatures.

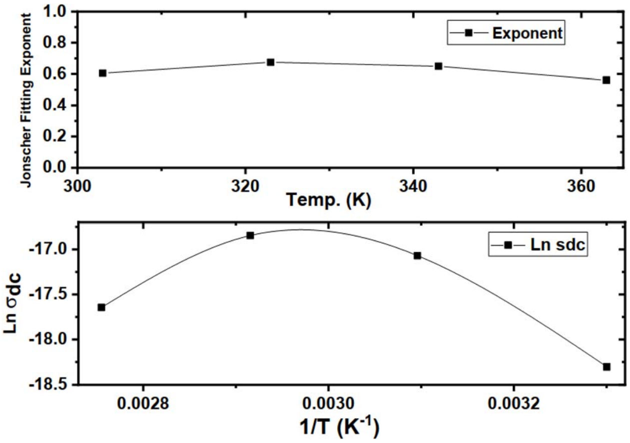

Fig. 12 Jonscher fitting exponent of S1 *versus* temp. in upper graph and Ln $\sigma_{dc}$ *versus* 1/*T* (K) in lower graph.

combined the two conduction mechanisms into one, as shown in the higher temperatures.

In Fig. 11, Jonscher conductivity fitting for S1 exposed the electrode polarization occurring in the composite as a decrement in the conductivity below the dc fitting line, indicating ionic conduction and double layer formation at the electrodes, which reveals itself in the hike at low frequencies in the permittivity curve. On the other hand, the Al effect, Fig. 8, appears in S2 through maximizing both the intensity and frequency range of the electrode polarization to consume about half the measured frequency window, leaving the rest of the frequency range to the dc conductivity. This means the exponential conductivity growth with frequency no longer exists.

Fig. 12 shows Jonscher fitting exponent of S1 in the upper part. It displays values in relation to temperature ranging from 0.5 to 0.7. It does not show a considerable change with temperature. This range points out that the correlated barrier hopping is the dominant charge conduction mechanism, where charges are hopping among barriers within the composite.

DC conductivity of S1 *versus* temperature, drawing the natural log of $\sigma_{dc}$ *versus* the inverse of Kelvin temperature. The relationship is nonlinear, *i.e.* not Arrhenius, which suggests more than one mechanism of conduction within the composite. Jonscher fitting and the hike in permittivity in the low frequency range indicate the presence of ionic conduction by electrode polarization. Finally, it can be said that two conduction mechanisms are involved here: correlated barrier hopping and electrode polarization.[56] The inclusion of CDs as a host for the ferrite, copper, and Aluminium has introduced a lot of merits to the composite, especially for the electrical characteristics and widened its applications. Generally, permittivity increase allows the composite to work in energy storage applications. Loss increment, low impedance, and high conductivity qualify for supercapacitor applications. According to the Cole–Cole plots of impedance and conductivity, the composite can be used as a negative temperature sensor for biosystems up to 70 °C.

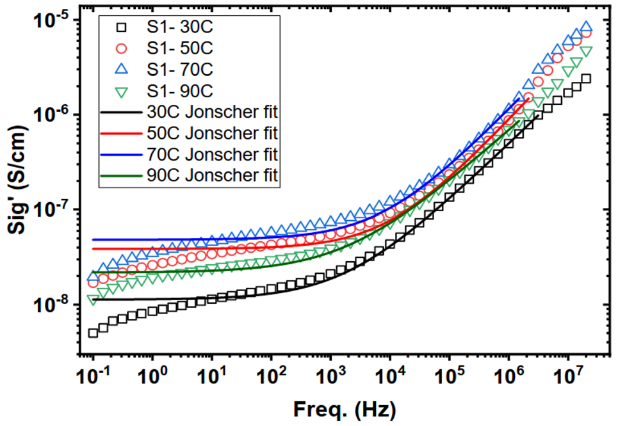

Fig. 11 Conductivity curves of S1 for various temperatures and their Jonscher fitting.

In summary of the electrical characteristics, the observed transition from insulating to semiconductor-like behavior, particularly the increase in AC conductivity with temperature (as discussed below Fig. 9), can be primarily attributed to the hopping mechanism of charge carriers, electrode polarization, and, at higher frequencies, short-range grain relaxation processes. The electrical transport in the composite is governed by a Maxwell–Wagner-type hopping mechanism combined with interfacial polarization, phenomena that are widely reported in ferrite-based composites (as noted in the Introduction and supported by previous studies on substituted ferrites; ref. 38, 41, 42, 44, and 45).

The incorporation of Al and Cu dopants introduces structural defects and modifies the electronic band structure of the carbon dots, leading to the formation of additional localized energy states. Consequently, charge carriers (electrons or polarons) can hop between these localized states, such as $Fe^{2+}$/$Fe^{3+}$ sites in magnetite and defect-induced states within the carbon dots.

The impedance and permittivity behaviors strongly support this transport mechanism. First, the observed decrease in impedance with increasing frequency and temperature results from the enhanced hopping frequency of charge carriers, which facilitates charge transport and reduces overall resistance. Second, the high dielectric permittivity ($\varepsilon'$) at low frequencies originates from interfacial polarization (Maxwell–Wagner effect) at the interfaces among carbon dots, $Fe_3O_4$-GO, and the hydrogel matrix. As the frequency increases, charge carriers are unable to follow the alternating electric field, leading to a gradual decrease in $\varepsilon'$. Notably, the four-order-of-magnitude increase in permittivity upon Al doping is attributed to the higher density of localized charge carriers and the formation of a more effective interfacial polarization network, confirming the successful incorporation of Al/Cu dopants.

The insulating-to-semiconducting transition is mainly driven by Al doping, which introduces excess electrons and vacancy defects following nitrate evaporation. These defects generate additional hopping pathways consistent with the correlated barrier hopping (CBH) model, as indicated by Jonscher's power-law exponent (0.5–0.7). The presence of defect states effectively bypasses the wide bandgap (~5.02 eV), enabling enhanced charge transport. This mechanism correlates well with the four-decade increases in both permittivity ($\varepsilon'$) and AC conductivity ($\sigma$_ac), along with the pronounced reduction in impedance from the MΩ range to several hundred ohms, as shown in Fig. 7–9. Furthermore, Cole–Cole plots reveal two relaxation processes, electrode polarization and bulk hopping, which gradually merge at elevated temperatures. The modulation of the electronic structure by Al doping enables stable semiconductor-like behavior up to 70 °C, as evidenced by the non-Arrhenius temperature dependence of DC conductivity and the substantial enhancement in permittivity.

In the broader context, significant research efforts are focused on modifying cellulose, an abundant bio-waste material, for use in electronic components, electromagnetic shielding, antistatic devices, and interfacial connections, provided that stable impedance can be achieved over a suitable frequency range. For instance, Tohamy *et al.* (2023) reported carboxymethyl cellulose blended with carbon nanotubes/Ag as an eco-friendly candidate for lithium-ion batteries, achieving an impedance of approximately 5 Ω and a conductivity of ~0.7 mS $cm^{-1}$.57 Earlier, Sohaimy and Isa (2015) demonstrated that doping carboxymethyl cellulose with ammonium carbonate reduced bulk resistance and increased conductivity from $9.33 \times 10^{-9}$ to $7.7 \times 10^{-6}$ S $cm^{-1}$ using 7 wt% dopant.[58] More recently, El-Nasharty *et al.* (2025) reported an increase in conductivity from $\sim 5 \times 10^{-5}$ to $\sim 10^{-3}$ S $cm^{-1}$, accompanied by a reduction in impedance from $\sim 10^4$ Ω to ~200 Ω.[37]

Accordingly, the present work represents a continuation of these efforts, emphasizing the use of bio-waste materials and green chemistry approaches to develop sustainable composites with electrical properties suitable for electronic and functional device applications.

Increasing permittivity leads to higher capacitance and allows for energy storage applications. In addition, a rise in the loss and conductivity of the dielectric materials alongside permittivity permits their use in supercapacitor applications. Also, escalating permittivity and conductivity allow for the use of such materials in electromagnetic shielding, as the higher permittivity materials cause increased refractions, reflections, absorption, and changes to the wavelength of the electromagnetic field. The absorption and reflection of electromagnetic fields protect sensitive electronic components like ICs.[59–61]

## Conclusion

In this work, a novel method for the *in situ* synthesis of Al/Cu-doped carbon dots within a $Fe_3O_4$-GO-CMC-AMPS hydrogel matrix was developed and characterized. The use of renewable resources like sugarcane bagasse for CMC and GO production highlights a sustainable approach in nanomaterial fabrication to achieve a superior multifunctional composite material with tailored electrical properties. Structural, morphological, and electrical analyses confirmed the successful formation and uniform distribution of doped carbon dots. The strategic incorporation of aluminum and copper doping, coupled with the unique properties of the $Fe_3O_4$-GO and hydrogel components, enhancing the composite's dielectric properties and electrical conductivity. Notably, aluminum doping significantly reduced impedance and increased both permittivity and conductivity, transitioning the material from insulating to a semiconductor-like behavior at certain temperatures. The observed increase in permittivity and conductivity, along with reduced impedance, highlights the potential of this composite for advanced applications ranging from supercapacitors and electromagnetic shielding to negative temperature sensors for biosystems.

However, some limitations of this work should be acknowledged. The stability and long-term durability of the composite under diverse environmental and operational conditions were not fully explored, which are critical for practical device implementation. The optimization of doping concentrations, synthesis parameters, and scaling up the microwave-assisted process require more detailed investigation to ensure reproducibility and efficiency. Additionally, while structural and electrical properties were comprehensively studied, optical behavior and in-depth electrochemical performance (*e.g.*, specific capacitance, cycling stability, energy density) were not fully explored and require further work to benchmark against state-of-the-art systems to fully establish the material's competitiveness. Future investigations aimed at resolving these limitations, optimizing the synthesis parameters, doping concentrations, evaluating long-term stability, and exploring potential applications for this promising composite in advanced technological solutions.

## Author contributions

Hebat-Allah S. Tohamy: writing – original draft, investigation, resources, conceptualization, methodology, funding acquisition. Mohamed El-Sakhawy: writing – review & editing, supervision, investigation. Azhar M. Elwan: investigation, methodology, resources, conceptualization, formal analysis, writing – review & editing.

## Conflicts of interest

The authors declare that they have no known competing financial interests or personal relationships that could have appeared to influence the work reported in this paper.

## Data availability

All experimental data supporting the findings of this study are included within the article. Additional datasets generated and analyzed during the current study are available from the corresponding authors upon reasonable request.

## Acknowledgements

This article did not receive any specific grant from funding agencies in the public, commercial, or not-for-profit sectors. The authors would thank the National Research Centre for technical support.

## References

1 A. Ali and A. Andriyana, *RSC Adv.*, 2020, **10**, 16390–16403.
2 M. M. AbdelMohsen, H.-A. S. Tohamy, H. M. El-Masry, W. E. Abd-Allah and M. El-Sakhawy, *Polym. Bull.*, 2025, **82**, 6629–6643.
3 S. A. Al Kiey and H.-A. S. Tohamy, *J. Energy Storage*, 2024, **101**, 113758.
4 M. El-Sakhawy, S. A. Abdel-Halim, H.-A. S. Tohamy, H. M. El-Masry and M. M. AbdelMohsen, *J. Renewable Mater.*, 2025, **13**, 981–995.
5 M. El-Sakhawy, H.-A. S. Tohamy, M. M. AbdelMohsen and M. El-Missiry, *J. Thermoplast. Compos. Mater.*, 2024, **37**, 2035–2050.
6 H.-A. S. Tohamy, *Sci. Rep.*, 2025, **15**, 32667.
7 D. Ozyurt, M. A. Kobaisi, R. K. Hocking and B. Fox, *Carbon Trends*, 2023, **12**, 100276.
8 S. Mottola, *et al.*, *J. Environ. Manage.*, 2024, **370**, 122714.
9 H.-A. S. Tohamy, *J. Renewable Mater.*, 2024, **12**(12).
10 H.-A. S. Tohamy, *Gels*, 2024, **10**, 296.
11 H.-A. S. Tohamy, *Sci. Rep.*, 2025, **15**, 30235.
12 H. Ren, F. Qi, X. Feng, J. Liu and Y. Zhao, *Molecules*, 2024, **29**, 5317.
13 H.-A. S. Tohamy, *Foods*, 2025, **14**, 2791.
14 L. Cui, X. Ren, M. Sun, H. Liu and L. Xia, *Nanomaterials*, 2021, **11**, 3419.
15 H.-A. S. Tohamy, M. El-Sakhawy and S. Kamel, *J. Renewable Mater.*, 2022, **10**, 1889–1909.
16 T. Churam, P. Usubharatana and H. Phungrassami, *Sustainability*, 2024, **16**, 2352.
17 H. Elsayed, H.-A. S. Tohamy, M. El-Sakhawy, M. El-Khateeb and E.-S. H. Nashy, *Environ. Monit. Assess.*, 2025, **197**, 894.
18 R. R. Kurhade, M. S. Shaikh, V. Nagulwar and M. A. Kale, *Int. J. Polym. Mater. Polym. Biomater.*, 2025, **74**, 1043–1067.
19 H.-A. S. Tohamy, *Sci. Rep.*, 2025, **15**, 741.
20 H.-A. S. Tohamy, *Gels*, 2024, **10**, 686.
21 H.-A. S. Tohamy, in *Recent Advances in Nanomedicines Mediated Wound Healing*, Elsevier, 2025, pp. 109–129.
22 H.-A. S. Tohamy, in *Quantum Dot Nanocarriers for Drug Delivery*, Elsevier, 2025, pp. 363–384.
23 E.-S. A. Haggag, H.-A. S. Tohamy, A. E. D. Mahmoud, M. El-Sakhawy and A. R. Salem, *Int. J. Biol. Macromol.*, 2025, 145666.
24 A. F. Sonsin, S. M. Nascimento, I. M. B. Albuquerque, E. C. Silva, J. C. A. Rocha, R. S. Oliveira, C. D. A. E. Barbosa, S. T. Souza and E. J. Fonseca, *RSC Adv.*, 2021, **11**, 2767–2773.
25 H.-A. S. Tohamy, A. Darwish, M. El-Sakhawy, G. Turky and S. Kamel, *ECS J. Solid State Sci. Technol.*, 2025, **14**, 031007.
26 W. C. H. Silva, M. A. Zafar, S. Allende, M. V. Jacob and R. Tuladhar, *Mater. Circular Econ.*, 2024, **6**, 23.
27 R. K. Singh, R. Kumar and D. P. Singh, *RSC Adv.*, 2016, **6**, 64993–65011.
28 L. Zhang, *et al.*, *Talanta*, 2025, **285**, 127365.
29 J. Fan, L. Kang, X. Cheng, D. Liu and S. Zhang, *Nanomaterials*, 2022, **12**, 4473.
30 G. Huang, *et al.*, *RSC Adv.*, 2017, **7**, 47840–47847.
31 K. Kasinathan, S. Samayanan, K. Marimuthu and J.-H. Yim, *Appl. Surf. Sci.*, 2022, **601**, 154266.
32 N. Kobylinska, D. Klymchuk, O. Khaynakova, V. Duplij and N. Matvieieva, *Nanomaterials*, 2022, **12**, 4231.
33 S. K. Ali, *et al.*, *Eur. Phys. J. Plus*, 2025, **140**, 24.
34 S. D. Priyadharshini, *et al.*, *Environ. Pollut.*, 2022, **306**, 119377.
35 H.-A. S. Tohamy, *Sci. Rep.*, 2025, **15**, 10337.
36 M. Yavari-Gohar, K. Kabiri, M. Zohuriaan-Mehr and S. Hashemi, *J. Polym. Res.*, 2010, **17**, 151–159.
37 M. El-Nasharty, M. El-Sakhawy and H.-A. S. Tohamy, *Sci. Rep.*, 2025, **15**, 19754.
38 G. Gallareta-Olivares, *et al.*, *Chemosphere*, 2023, **312**, 137190.
39 S. Yılmaz, Y. Atasoy, M. Tomakin and E. Bacaksız, *Superlattice. Microstruct.*, 2015, **88**, 299–307.
40 S. Padhan, T. K. Rout and U. G. Nair, *Colloids Surf., A*, 2022, **653**, 129905.
41 C. Lou, *et al.*, *J. Mater. Res.*, 2019, **34**, 2964–2975.
42 I. Ganesh, *et al.*, *Appl. Surf. Sci.*, 2014, **293**, 229–247.
43 X. Li, M. Rui, J. Song, Z. Shen and H. Zeng, *Adv. Funct. Mater.*, 2015, **25**, 4929–4947.
44 N. Kumari, V. Kumar and S. Singh, *Int. J. Mod. Phys. B*, 2014, **28**, 1450210.
45 M. Amir, H. Erdemi, M. Geleri and A. Baykal, *J. Supercond. Novel Magn.*, 2016, **29**, 389–400.
46 H.-A. S. Tohamy, M. El-Sakhawy, S. A. Abdel-Halim, H. M. El-Masry and M. M. AbdelMohsen, *Euro-Mediterr. J. Environ. Integr.*, 2025, **10**, 2007–2018.
47 W. Sharmoukh and H.-A. S. Tohamy, *Waste Biomass Valorization*, 2025, 1–12.
48 H.-A. S. Tohamy, *Sci. Rep.*, 2025, **15**, 19335.
49 H. D. Hassanein, H.-A. S. Tohamy, M. M. AbdelMohsen, H. M. El-Masry and M. El-Sakhawy, *Egypt. J. Chem.*, 2025, **68**, 287–294.
50 F. E.-Z. S. Mohamed, H.-A. S. Tohamy and M. El-Sakhawy, *BMC Pharmacol. Toxicol.*, 2025, **26**, 94.
51 H.-A. S. Tohamy, A. Koriem and D. E. El-Nashar, *BMC Chem.*, 2025, **19**, 239.
52 H.-A. S. Tohamy, *et al.*, *Int. J. Biol. Macromol.*, 2024, **261**, 129801.
53 A. Lakshmi Devi, M. Sreelakshmi, P. Suneesh and T. Satheesh Babu, *Sci. Rep.*, 2025, **15**, 1262.

54 M. Najaflu, M. Shahgolzari, F. Bani and A. Y. Khosroushahi, *ACS Omega*, 2022, **7**, 34573–34582.

55 G. Ramanathan, S. V. Rathan and K. Murali, *SN Appl. Sci.*, 2019, **1**, 116.

56 M. Sassi, A. Bettaibi, A. Oueslati, K. Khirouni and M. Gargouri, *J. Alloys Compd.*, 2015, **649**, 642–648.

57 H. S. Tohamy, M. El-Sakhawy and M. M. M. Elnasharty, *Diamond Relat. Mater.*, 2023, **138**, 110205.

58 M. I. H. Sohaimy and M. I. N. Isa, *Appl. Mech. Mater.*, 2015, **719–720**, 67–72.

59 A. G. Webb, *Concepts Magn. Reson., Part A*, 2011, **38A**, 148–184.

60 J. Riebesell, T. W. Surta, R. E. A. Goodall and M. W. Gaultois, *Cell Rep. Phys. Sci.*, 2024, **5**, 102012.

61 J.-W. Zha, M.-S. Zheng, B.-H. Fan and Z.-M. Dang, *Nano Energy*, 2021, **89**, 106438.